RESEARCH PAPER

Open-source support toward validating and falsifying discrete mechanics models using synthetic granular materials—Part I: Experimental tests with particles manufactured by a 3D printer

Ritesh Gupta[1] · Simon Salager[1] · Kun Wang[2] · WaiChing Sun[2]

Abstract

This article presents a new test prototype that leverages the 3D printing technique to create artificial particle assembles to provide auxiliary evidences that supports the validation procedure. The prototype test first extracts particle shape features from micro-CT images of a real sand grain and replicates the geometrical features of sand grain using a 3D printer. The quantitative measurements of the particle shape descriptors reveal that the synthetic particles inherit some attributes such as aspect ratio and sparseness of the real materials while exhibiting marked differences for sphericity and convexity. While it is not sufficient to consider the printed particle assembles a replica of the real sand, the repeatable manufacture process provides convention tools to generate additional data that supports the validation procedure for particulate simulations. Oedometric compression tests are conducted on a specimen composed of the printed particles of identical size and shape to create benchmark cases for calibrating and validating discrete element models. Results from digital image correlation on the synthetic sand assemblies reveal that the fracture and fragmentation of the synthetic particles are minor, which in return makes particle position tracking possible. As our prototype test and research data are designed to be open source, the dataset and the prototype work will open doors for modelers to design further controlled experiments using synthetic granular materials such that the individual influence of each morphological feature of granular assemblies (e.g., shape and size distribution, void ratio, fabric orientation) can be individually tested without being simultaneously affected by other variables.

1 Introduction

Dry granular materials are conglomerations of particles characterized by energy dissipation due to granular interaction and rearrangement of configurations. In many geotechnical and geomechanics engineering applications, the macroscopic responses of the granular materials under confining pressure are of particular interest [17, 33, 37, 40, 53]. Hence, a significant amount of theoretical and numerical models have been proposed to predict the constitutive responses, such as shear strength, compressive strength, and bearing capacity of a representative specimen, under different loading conditions. Using internal variables to represent the strain history of a material point, the calibration and validation of these models require data from a macroscopic test performed on a homogeneous or nearly homogeneous specimen. Nevertheless, the particulate nature and grain size distribution of the granular materials often leads to inherent spatial heterogeneities of void ratio, porosity, the angle of friction, and specific gravity, which makes the homogeneity assumption invalid and the predictions of the macroscopic constitutive model less robust.

✉ WaiChing Sun
wsun@columbia.edu

1 Univ. Grenoble Alpes, CNRS, Grenoble INP, 3SR, 38000 Grenoble, France

2 Department of Civil Engineering and Engineering Mechanics, Columbia University, 614 SW Mudd, Mail Code: 4709, New York, NY 10027, USA

While the recent advancements of micro-mechanical modeling techniques, such as the distinct or discrete element method (DEM), have offered new ways to more explicitly incorporate some of these microstructural effects in numerical predictions [9], the calibration and validation of these micro-mechanical models are often limited by the availability of experimental data at the grain scale [24, 27]. As a result, calibration and validation of these micro-mechanical models often lead to excessive tuning of material parameters to match the macroscopic stress–strain curves and the state path obtained from macroscopic experiments. As demonstrated in Wang et al. [52], the drawback of this approach is that the material parameter identification procedure is often under-constrained. Unlike the macroscopic phenomenological models in which strain histories are represented by one to several internal variables, a micro-mechanical model often employs much more information in the calibration stage. This information can be related to particle morphology (e.g., particle positions, shape, size, packing, fabric orientation) and micro-mechanics material behaviors (surface roughness, fracture energy). In most cases, only a subset of this large amount of calibration data is available. An undesirable consequence is that it often leads to a very high flexibility to curve-fit the same macroscopic constitutive responses with different combinations of microstructures and constitutive laws. This arbitrariness, which is sometime referred as the curse of high dimensionality (cf. Friedman [14]), has led to calibrated micro-mechanical DEM model deprived of true prediction power [52].

The purpose of this paper is to present a simple, practical, and reproducible experimental prototype that employs 3D printing and micro-CT technique to resolve this under-constrained issue and help assessing the quality of DEM simulations in controlled tests. While we acknowledge that replicating the constitutive responses of a sand assembly using manufactured particles would be an interesting exercise, this paper is not focusing on perfecting the additive manufacture technique to make this important but difficult task possible. Such a pursuit would require far more detailed quality control and more advanced manufacture technology to ensure that each manufactured particle and the natural counterpart have almost identical mechanical properties (e.g., elastic moduli, fracture toughness, frictional coefficient of the surface) and is therefore out of the scope of this study. Rather, our focus is provide a simple way to leverage 3D printing technique to create artificial scenarios in which the additional (but limited) controls afforded by manipulating the properties of 3D printing particles can provide sufficient information to analyze the robustness, accuracy and forward prediction capacity of discrete element models. In particular, as the addictive manufacture process provides the users great flexibility in manipulating the grain size distribution, selecting the raw materials and changing the particle shapes, one may introduce experiments performed on artificial granular assemblies composed of synthetic particles with controllable sizes, shapes and forms.

This latter point is highly relevant for models used to make forward predictions, as it is quite common to attribute the failure of calibration and validation of DEM models on the discrepancy on GSD, mineralogy of grains and grain shapes. However, such a claim is not meaningful if one cannot quantify the influences of these morphological characteristics in sufficiently controlled environments. The 3D printing techniques therefore provide us a convenient way to create such evidences with multiple granular assembles essentially composed of the same set of particles manufactured at different production cycles.

As a starting point, we present our design of reproducible tests that include five simple steps, i.e., (1) extracting the geometry of a single particle from micro-CT imaging and reconstruction, (2) converting the micro-CT images into finite element mesh and STL (Standard Tessellation Language) file for 3D printing, (3) performing quality control and preparation step to create synthetic particles (4) conducting macroscopic mechanical tests accompanied with micro-CT imaging and (5) post-processing with discrete digital image correlation (DDIC; cf. Ando et al. [2], Andò et al. [1], Matuttis et al. [25]) to track each and individual particle movement while measuring the macroscopic stress–strain responses. Upon completion, this series of steps will provide not only more experimental data but the right category of data specifically targeted for micro-mechanical model calibration and support. More importantly, the data generated from the tests are open source such that they can be used to support blind tests by a third party.

2 Background

Previous works on granular materials over past two decades have explored the relationships between particle morphological features and macroscopic constitutive responses [4, 5, 7, 12, 16, 19, 21, 23–25, 28, 29, 39–41, 47–52].

For instance, Shin and Santamarina [38] study the role of particle shape using mixtures of two different shape grains of sands and reported a significant difference in shear strength under similar experimental conditions. Matuttis et al. [25] numerically investigate particle morphology using spherical and elongated particle configurations and highlighted its effect on mechanical response with additional emphasis on the significance of inter-particle friction.

Nouguier-Lehon et al. [28] use 2D DEM simulations to study how morphological features, such as angularity, affect the initial specimen anisotropy. Their study indicates that the initial specimen anisotropy and the angle of internal friction are all higher for assembles composed of elongated grains than the isotropic counterpart. Cho et al. [7] investigate two experimental databases to explore the effects of particle shape on packing density and on the small-to-large strain mechanical properties of sandy soils and reported an increase in critical state friction angle (ϕ^c) and compressibility under zero-lateral strain loading (C_c) with increasing particle irregularity.

They also indicate some particle-level mechanisms associated with particle irregularity responsible for particular macroscale response, like hindered rotation, slippage, and the ability for particle rearrangement, lower inter-particle coordination, increased particle-level dilation, lower contact stiffness, and higher proneness to contact damage. They further highlighted that particle shape emerges as a significant soil index property that needs to be properly characterized and documented for a better understanding of granular behavior. Pena et al. [32] study the influences of particle shape on the global mechanical behavior of dense granular media using 2D molecular dynamics simulations of periodic shear cells. Their simulation results indicate that assemblies composed of elongated grains often form thicker shear band due to their tendency to move along preferential orientations with less rotation than the spherical-grain counterpart. Oda et al. [30] also report that the fabric tensor, a representative of the geometrical structure of the force chain, aligns to the principal stresses for isotropic grains, but possess different spectral directions of the stress tensors for assembles composed of elongated particles. Athanassiadis et al. [5] utilize a 3D printing technique to produce 3D printed particles for triaxial compression experimental tests on specimens composed of particles of 14 different shapes reconstructed from statistic information. Their findings reveal significant dependence of macroscopic elastic modulus, stress path, and plastic behavior on the particle shape descriptors, such as the particle sphericity and contact preference parameters.

On the other hand, the influences of particle shape and size distribution on the macroscopic responses have been studied via numerical simulations. For example, Favier et al. [12] and Katagiri et al. [19] present a DEM model that lumps multiple spherical grains to form aggregates to represent axi-symmetrical, smooth-surfaced, non-spherical particles. This approach enables one to reuse most of the standard DEM techniques, such as contact detection algorithm for spherical particles and hence greatly simplifies the implementation. Andrade et al. [4] introduce a level-set-based discrete element model, which is referred as granular element method (GEM), that allows discrete elements to take realistic and complex (instead of simple geometrical) granular shapes of real geo-materials (e.g., sand grains). Using non-uniform rational basis splines (NURBS) technique. Miskin and Jaeger [26] study the impact of particle shape on mechanical response through artificially evolved granular materials from different arrangements of lumps made of spheres.

Hanaor et al. [16] introduce three methods, such as fractal surface overlay (FSO), contour rotation interpolation (CRI), and directed polyhedral aggregation (DPA) based on quantitative extraction of some input parameters from real grain to numerically reproduce particles having shape features similar to that of a real grain. This approach enables the quantitative characterization of grain morphological features represented by proper reduced-order bases. In addition, they used model grains produced from CRI method for 3D printing and studied two types of geometrical shapes namely rough spheres and rough-and-angular spheres with triaxial compression, reporting the considerable difference in response owing to shape parameter. In essence, these three methods have potential to enable investigation mainly emphasizing shape parameter by simply changing the corresponding input parameter and observing the subsequent macroscale response of tested specimen. As a result, readers interested at using 3D printing technique to study morphological characteristics is referred to Hanaor et al. [16] in which morphological features obtained from experimental data are extracted and simulated grains are reconstructed using fractal surface overlay (FSO), contour rotation interpolation (CRI) or directed polyhedral aggregation (DPA). Another shape descriptor approach has also been recently proposed by Ouhbi et al. [31] in which proper orthogonal decomposition (POD) is performed on digitized particles to extract geometrical features or descriptors.

In this work, our purpose is not analyzing the importance of particle shape effect. Rather, our goal is merely to introduce an approach to create artificial assembles composed of particles of controllable shapes and sizes to support benchmark and validation produces. As such, we introduce a workflow that utilizes micro-CT images to manufactured 3D particles of identical size and shape and subsequently subjected this artificial assembles to one-dimensional confinement test. A micro-CT images of a real sand grain (Hostun Sand RF, for present studies) is provided to us by the laboratory 3SR, Drs. Edward Ando and Max Miebicke to create a benchmark test.

In the proposed workflow, we first bypass the usage of statistical descriptors and directly compute and use the signed-distance function of micro-CT images to create 3D grains of the identical geometry of a real sand grain.

Second, our goal here is not using 3D printing to generate realistic granular assemblies. Rather, our intention is to conduct control experiments in which we explore how artificial granular assemblies composed of grains of identical particle shape might behave mechanically. As such, we also study the limitation of the 3D printing techniques and directly compare the morphological differences between the real and artificial grains. Following that, we use digital image correlation to track the displacement and rotation of each particle in specimen over the course of mechanical loading. Here, the goal of particle tracking is to establish a statistical database of individual particle movement which will serve as a right category of data to aid the calibration and validation of DEM models.

3 Additive manufacture of synthetic particles from micro-CT images

In this section, the detailed process of producing synthetic particles from 3D printers has been described. First, an image segmentation is performed using nano-tomographic imaging on a single Hostun Sand RF sand grain (cf. Flavigny et al. [13] for physical properties) to extract the geometry (at 1 μm resolution) of a particle (Fig. 1a) as a 3D image stack provided by collaborator Edward Ando and Max Wiebicke from laboratory 3SR.

Secondly, the voxel image stacks are converted into a signed-distance function using a semi-implicit level-set scheme (cf. Sun et al. [39, 42]). The usage of the signed-distance function, as opposed to the original binary images, is essential as one may easily adjust the thickness of the particles. This signed-distance function provides a guideline to generate the point cloud that represents the geometry of the surface of the grain. Following this step, a surface mesh is first generated using the CDT (constrained Dalaunay tetrahedralization) approach (cf. Fang and Boas [11]) , followed by the creation of unstructured volumetric mesh (Fig. 1b). Typically, the volumetric mesh generated from this procedure might not be printable. For instance, the 3D model may contain gaps in faces or edges, or it may contain isolated edges or vertices. In other cases, the point cloud might be too concentrated in a very small region in an attempt to capture the details of complex morphological features. In those cases, we use an open-source software Meshlab to repair the model and examine the correction manually. Once this is completed, the mesh can be converted into an STL file which is then used as the input file for the 3D printer. It should be noted that once the 3D mesh and the STL file are created, the manufacturing process of the 3D synthetic particle is reproducible.

The STL format input file for a 3D printer is reviewed again for printability through the manufacturer's 3D printing software to go through a "solidity check". This check is most critical to perform before moving on to actual printing. It highlights the surface of the particle as a color pattern showing delicate parts (as red) which are not fit for quality printing (i.e., areas having wall thickness lower than the minimum threshold of 1 mm). This check gave negative results for desired 10 times up-scaled grains (i.e., max. grain size 3.0 mm) as shown in Fig. 1c presenting many delicate parts in the grain surface. Hence, some modification named as "critical areas thickening" was carried out by the manufacturer. The thickening process altered the scale of originally desired grain (i.e., $2.5 \times 3.0 \times 2.4$ mm) and a slightly bigger grain with scale $3.1 \times 3.7 \times 3.0$ mm was found fit for quality printing (Fig. 1d) within an acceptable uncertainty. The synthetic particles were produced using SLS (Selective Laser Sintering) printing method on plastic constituent material Fine Polyamide PA 2200 (tensile modulus $= 1700 + 150$ MPa, sintered material density $= 0.90$–0.95 g/cc, manufacturer = SCULPTEO). Quality printing output was assured with the fine printing layer thickness (60 μm). The raw surface finish was chosen to ensure the consistent surface
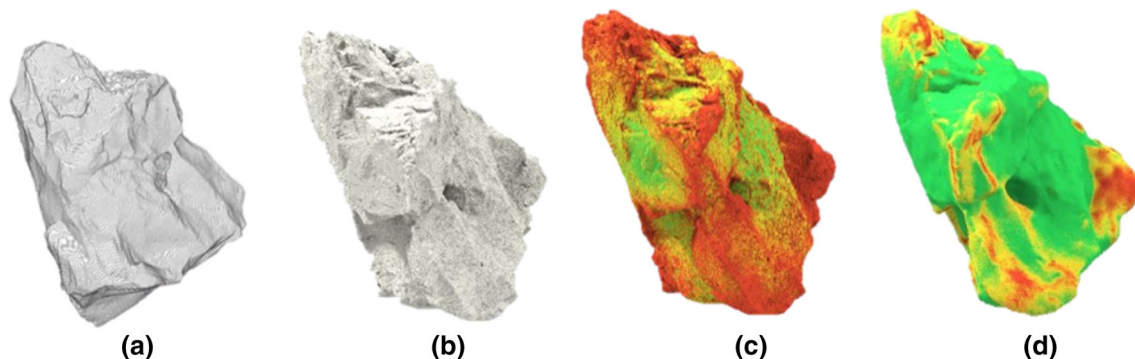

Fig. 1 Grain printing process **a** 3D view of image stack obtained after X-ray CT and image processing; **b** tetrahedral mesh output using CDT approach; **c**, **d** solidity check for original and modified design respectively; (red—too thin, yellow—susceptible to break and green—ready for printing) (color figure online)

characteristics for all grains which would have been susceptible to the polished surface.

Lastly, it is important to know that 3D printing is a very costly work with around 5–10 USD for a single-grain printing. For present studies, we needed around 3000 grains, and at this rate, the production would have been highly expansive and uneconomical. This issue was dealt with by using "boxes printing" approach (Fig. 2) allowing to print 100 grains together in a box instead of one single particle. This approach utilizes the characteristic of SLS printing method where all grains in a box are physically separated by easily removable not sintered plastic powder resulting 100 individually separable grains in each box. The cost of one box printing was same as that of individual grain printing and thus the production costs drastically reduced by 100 times.

The raw materials we used to manufacture the synthetic particles is Ployamide 2200, a synthetic polymer commonly used for 3D printing. The mechanical properties of Ployamide 2200 are determined by the manufacturer SCULPTEO, which is available online. In particular, the Young's modulus of the Ployamide 2200 is 1250 ± 150 MPa, the shear modulus is 475 ± 25 MPa and the tensile strength is 45 ± 3 MPa. With this information, one may calculate the normal and tangential stiffness, k^n and k^t, via the Hertz's contact theory for modeling the non-adhesive contact in discrete element model (cf. Johnson and Johnson [18], Sun et al. [43], Kuhn et al. [21]), i.e.,

$$\mathrm{d}f^n = k^n \mathrm{d}\delta; \quad k_n = \frac{\sqrt{2}G\sqrt{R^e}}{1-v}\delta^{1/2} \tag{1}$$

$$\mathrm{d}f^t = k^t \mathrm{d}s; \quad k_s = \frac{\sqrt{2}G\sqrt{R^e}}{2-v}\delta^{1/2} \tag{2}$$

where $\mathrm{d}f^n$ and $\mathrm{d}f^t$ are the incremental change of the normal and tangential forces, $\mathrm{d}\delta$ and $\mathrm{d}s$ are the normal and tangential relative displacement, R^e is the effective radius of the particles. Nevertheless, one should notice that, the actual tangential force could be frictional. Yet, due to the

printing process may lead to a very rough surface, the frictional properties, abrasion, wear and the visco-elasto-plastic contact effect might need further experimental tests. Further experiments on the particle properties, the construction of proper inverse problems for material parameter identification at the specimen scale and the validation procedure is out of the scope of this study, but will be considered in the follow-up study.

4 Comparisons of the real and printed grain morphology

This section presents the quantitative comparisons on features of real and printed grains measured using image processing package FIJI, a forked version of ImageJ with additional functionality for morphological analysis [36]. The 3D image stack for printed grain (Fig. 3, right) was obtained using the same procedure as that for a real sand grain (at a different resolution = 10 μm though). The 3D image stacks for both real and printed grain, presenting their surficial characteristics, were compared based on the shape descriptors (see Wadell [46] for definition) measurement (see Table 1). These measurements were carried out using image processing tool ImageJ (FIJI) and validated through the same measurements on perfect sphere reporting unit magnitude for all shape descriptors.

The difference in sphericity indicates the higher angularity in printed grains in comparison with real grains. This observation is also evident from the scale change in printed process as described before. The convexity parameter indicates higher surface roughness for printed particles and thus justifies the raw surface finish used for printed grains.

In addition, some shape descriptors were measured based on ellipsoid fitting (Fig. 4). These set of measurements are indicators of particle geometry. The quantitative comparison indicates the significant geometrical
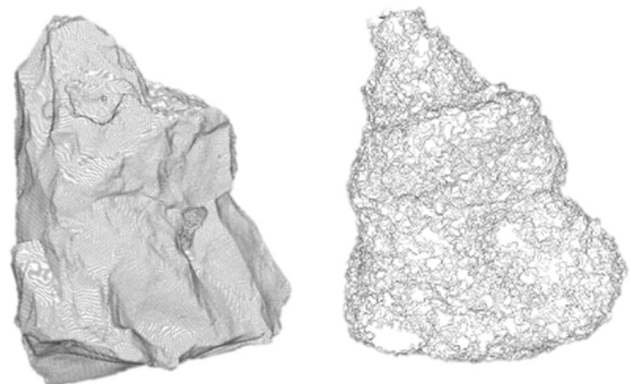

Fig. 2 3D printed grains using box printing method approach

Fig. 3 Real (left) and printed (right) grain image stack for shape feature measurement

Table 1 Quantitative measurements of particle shape descriptors

Shape descriptors	Real grain	Printed grain
Surface feature		
Sphericity	0.671	0.559
Convexity	1.534	1.980
Fitted ellipsoid parameters		
Elongation	1.446	1.554
Flatness	1.454	1.463
Aspect ratio	2.102	2.274
Spareness	0.818	0.850
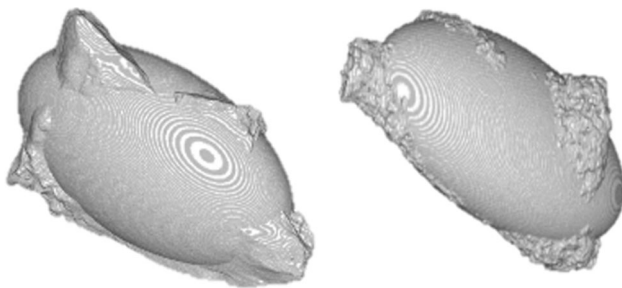
Fig. 4 Real (left) and printed (right) grain image stack based on ellipsoid fitting

differences in printed grains (e.g. more elongation, flatness and aspect ratio) in comparison with the real grain features. Most importantly, all parameters are dimensionless and thus are independent of particle scale and therefore allow better judgment of changes occurred during the printing process.

Moreover, as mentioned earlier and in previous work, such as Matuttis et al. [25], the shear strength of a particulate materials are significantly influenced by the particle morphology. Therefore, friction angle measurements in form of angle of maximum stability and critical state friction angle were carried out using methods described by Athanassiadis et al. [5] and Santamarina and Cho [35] respectively (see Table 2).

Table 2 Estimations of friction angles. The critical state frictional angle is estimated based on the procedure described in Santamarina and Cho [35], while the angle of maximum stability is determined following the procedure in Athanassiadis et al. [5]

Friction angles	Real grain assembly	Printed grain assembly
Angle of maximum stability	$37° \pm 3°$	$41° \pm 3°$
Critical state frictional angle	$27° \pm 3°$	$28° \pm 3°$

The higher angle of maximum stability ϕ^{m} for printed grains indicates higher surface roughness. Moreover, the larger particle size ($d_{max} = 3.7$ mm) of printed grains compared to real one ($D_{50} = 0.3$ mm, cf. Flavigny et al. [13]) and higher angularity results more stable granular interlocking and thus results in lesser displacement [5]. However, the critical state friction angle ϕ^{c} of the assembly estimated via the procedure in Santamarina and Cho [35] is very close to the reported value of Hostun sand. Due to the differences in grain size distribution, grain mineralogy, surface roughness, and the inherent heterogeneity, this result could be surprising. One possible explanation is that the porosity and particle shape might be the most dominated factor that influences the effective friction angle of the grain assembles. Hence, despite of the differences in particle size and mineralogy, the effective friction angle remains close. On the other hand, results of ring shear tests reported in Sadrekarimi and Olson [34] suggest that the critical state friction angle ϕ^{c} is primarily dependent on particle mineralogy and shape (angularity). Also, Xu and Sun [54] based on direct shear box test on sand reported that friction coefficient at critical state is only related to surface roughness as no volumetric deformations occur in this stage; and friction coefficient increases with increasing surface roughness. In our studies, a slightly higher ϕ^{c} for printed grains can be supported by this hypothesis as printed grains have more surface roughness than real sand grain (see Table 1, convexity). Moreover, Azeiteiro et al. [6] report critical state friction angle value of $31.5°$ for Hostun sand from a drained triaxial compression test and therefore exists a contradiction from our estimated results obtained via the simplified procedure in Santamarina and Cho [35].

It is important to note that we performed ϕ^{c} measurement on the real sand specimen having grains ranging from sieve 0.315 mm (passing) and 0.250 mm (retaining), resulting in an almost uniform grain size distribution and so as to make the comparative studies with the mono-disperse assembly of printed grains more reliable. Therefore, the contradiction between two ϕ^{c} measurements for real sand ($31.5°$ from previous tests [6] and $27 \pm 3°$ measured in present studies) can be explained from the different grain size distribution. In these circumstances, the critical state friction angle measurement for printed grain specimen may not be reliable but can be used on trial basis, since the execution of a triaxial test for ϕ^{c} measurement for printed grains is subjected to the ultimate strength of assembly which is out of the scope of present studies.

In conclusion, the morphological measurement and comparison serve three main purposes. (1) It allows convenient and reliable quantitative measurement of particle shape parameters directly from images (2) It enables us to

identify and highlight the surficial changes occurred in the printing process and (3) these quantitative data have the capability to fine-tune parameters to aid for calibration of DEM models.

5 Experimental campaign

The mechanical response of printed particles was investigated through a simple oedometer test accompanied by X-Ray CT setup on the dry specimen. The choice of studying specimen under simple stress conditions was to explore the limit of compressive strength without any breakage in printed particles. A cylindrical specimen 45.00 mm in diameter and 15.50 mm in height, comprising of 1522 similar shaped and sized particles were prepared using dry air pluviation [10] in an oedometer test setup developed in laboratory 3SR by previous researchers. Figure 5 presents a layout sketch of the experimental setup. Notably, the piston movement was in a positive vertical direction opposite to the conventional oedometer test. This was a requirement to conveniently use X-ray CT setup during the course of mechanical loading in strain-controlled (at 0.1% per minute speed) quasi-static conditions.

During the course of mechanical loading, 18 X-ray CT scans (at 28 μm resolution) were made up to 20% strain with two unloading steps from 10 to 7.80% and from 19 to 16% strain (see Fig. 6b). 3D image stacks presenting the position of each particle in the specimen (at different levels of imposed strain) were obtained from scanned X-ray radiographs using reconstruction software developed by RX Solutions.

Figure 6a presents the 3D reconstructed image of the specimen in the initial test condition. The printed particles in the specimen can be seen being identical, although there

could be some minor discrepancies and defects accumulated during the manufacturing process. A vertical slice cut in the middle of the sample is presented in Fig. 6b for "six" selected strain levels out of 18 scanned specimen states. The piston moment from bottom to top can be clearly seen in these vertical slices from the changing blank (white) area in bottom part of all 45×15.50 mm (not to scale) slices.

The one-dimensional response shown in Fig. 6b resembles those of a typical granular materials in which the one-dimensional elastic modulus is higher when the assembly is subjected to higher axial stress.

In addition, while tracking the particles in the micro-CT images, we observe that there is no significant breakage/cracks in grains even at 20% of vertical strain. This finding may be attributed to the high fracture toughness of the printed materials and the high initial porosity. Due to the lack of grain crushing, one may assume that the deformation of the printed grain assembles is mainly caused by grain rearrangements and porosity reduction. In the following sections, we discuss the behavior of printed particles at macroscopic and microscopic levels in greater details.

6 Analysis of macroscopic responses

The relation of void ratio vs. the vertical stress of the synthetic grain assembly is shown in Fig. 7. A visual inspection may indicate that the one-dimensional compression (K_o consolidation) curve of the synthetic grain assembly qualitatively resembles that of a typical granular materials. In total, there are 18 scan points at which X-ray micro-CT images are taken. During the X-ray imaging process, the axial strain is kept constant and the stress is
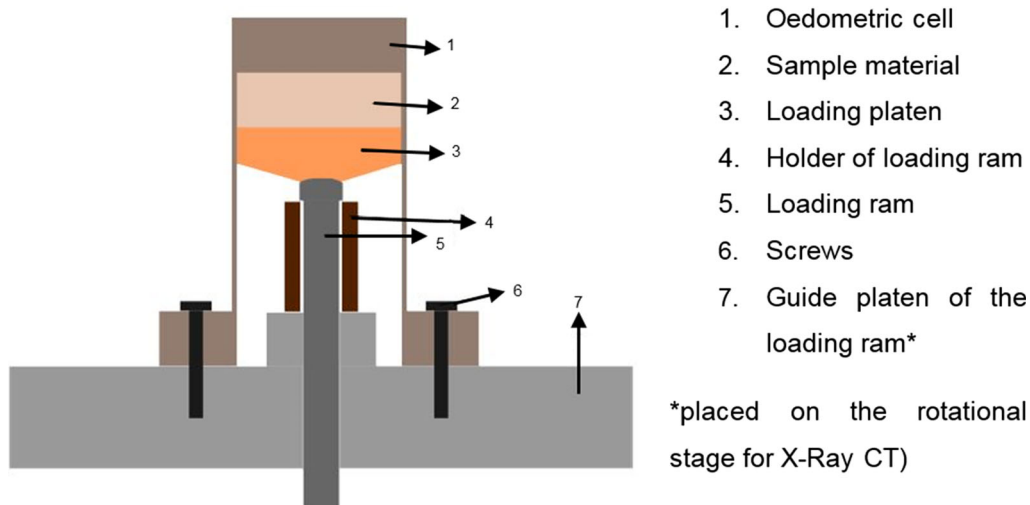

1. Oedometric cell
2. Sample material
3. Loading platen
4. Holder of loading ram
5. Loading ram
6. Screws
7. Guide platen of the loading ram*

*placed on the rotational stage for X-Ray CT)

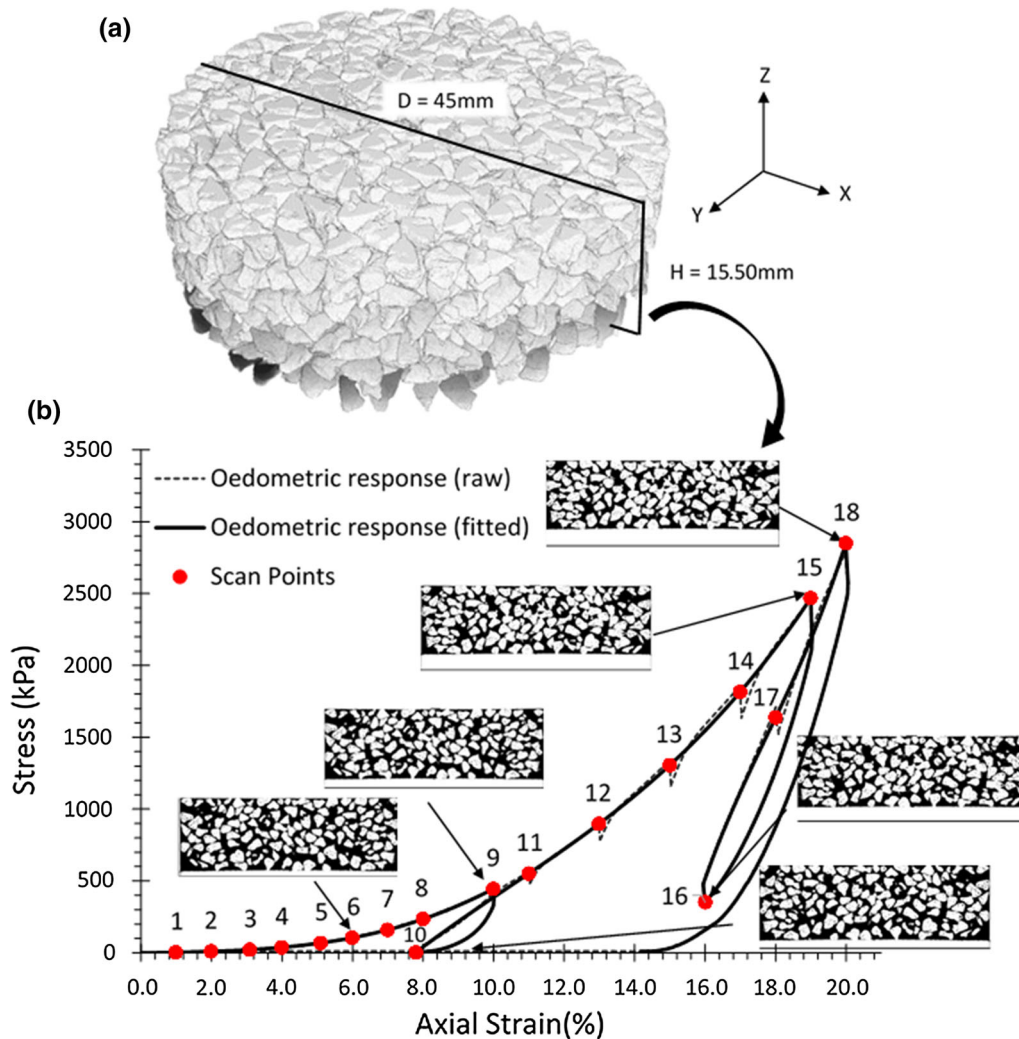**Fig. 5** Odeometer cell and its components

Fig. 6 **a** 3D view of reconstructed image stack from initial state of specimen, **b** vertical stress (kPa) and axial strain (%) plot for printed particles specimen under oedometric studies inclusive of X-ray CT relevant information

monitored. Our result shown in Fig. 7 indicates that there is stress relaxation and hence the constitutive response of the synthetic grain assembly is rate dependent. This rate dependence is particularly obvious when the vertical stress is low and during the virgin compression.

Strictly speaking, granular responses may exhibit rate dependence and that rate dependence may affect the measurement of constitutive responses. Our experimental results shown in Fig. 6, which is obtained at the strain rate of 0.1% per minute, exhibit stress relaxation which is consistent with the observation in the triaxial compression test conducted at Andrade et al. [3]. Nevertheless, we also found that the stress relaxation is less significant in our current study than those in Andrade et al. [3]. This evidence may suggest that the measurement of Cc and Ce is taken in a strain rate sufficiently close to maintain the quasi-static regime.

The filtered 1D compression curve shown in Fig. 7 is obtained via a nonlinear regression in which polynomial was fitted. The algorithm we used is from the curve fitting toolbox "cftool" in MATLAB. The data in raw experimental response plot was segmented in 5 parts; representing 3 loading and 2 unloading regimes. Data in each segment was treated separately for regression and combining them all produced the final plotted "fitted curve".

The compression (C_c) and recompression (C_e) indices of the synthetic grain assembly were inferred and shown in Table 3. The published results performed on Hostun sand assemblies in Colliat-Dangus [8], Lancelot et al. [22] were also included as reference points in Table 3. As the synthetic grain assembly is subjected to multiple loading/unloading cycle (see Fig. 7), the compression and recompressive indices are measured multiple times. According to Fig. 7, the recompression index seems to decrease each time the material is in the unloading/
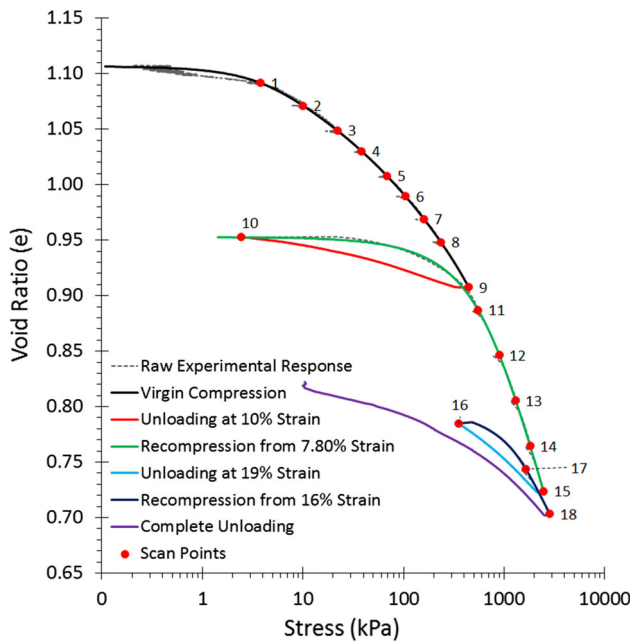
Fig. 7 Void ratio vs vertical stress of the synthetic grain assembly

(1250 $\pm$ 150 and 475 $\pm$ 25 MPa accordingly). This low modulus may also be related to the higher ductility exhibited in the synthetic materials and hence explains the lack of fracture and grain crushing. Another evidence we observed is from the image analysis where the correlation error for few grains is higher near the top and bottom interfaces. These errors are often attributed to (1) closely related gray values of grain and interface, and (2) small changes in shape of grain. Both these possibilities are indicated by search window error in DDIC results [2].

It should be noted that, unlike the real Hostun sand assemblies previously used in Colliat-Dangus [8], Lancelot et al. [22], the synthetic grain assembles are composed of grains of identical sizes and shapes. The fact that the particles are of the same size and shape makes the assembles extremely poorly graded. A well-known fact is that those materials often exhibit much lower dry density and hence easier to maintain higher void ratio when subjected to the compressive loading. However, this mechanism could be offset by the higher deformability of the plastic materials.

Furthermore, the synthetic sand is made of a plastic material, which exhibits different elasticity and critical energy release rate from the real Hostun particle counterpart. Surprisingly, the compression and recompression indices of the synthetic sand are quite close to those of the real material when the vertical strain is within 10%, as shown in Table 3. Since the only properties of the synthetic assemblies controlled in this experiment is the particle shape and the initial void ratio, this result seems to indicate that the particle shape may play an important role on the K_o consolidation process. As such, despite of the discrepancies in grain size distribution, particle surface roughness, particle bulk stiffness and the lack of inherent heterogeneity, the synthetic particle is able to replicate qualitatively but not quantitatively some key characteristics of K_o consolidation of the real sand counterpart. Whether this conclusion could be further generalized is not clear, but may warrant further investigations along this direction.

reloading cycle. This degradation is not significant in the first unloading/reloading cycle but becomes more apparent in the second and third one. This indicates that the material exhibit a elasto-plastic-damage coupling responses. In other words, if the constitutive response is purely elastoplastic, then one should expect that the recompression index for each unloading and reloading would remain identical, as indicated in Keller et al. [20].

Recall that our examination of the synthetic particles collected after the one-dimensional compression test does not reveal significant grain crushing. Hence, the apparent degradation does not seem to come from the grain crushing and the resultant pore collapse. Instead, this could be attributed to the fact that the synthetic particles made of plastic (PA 2200) is much more deformable than the real sand, as evidenced by the low bulk and shear moduli

Table 3 The compression index C_c and the recompression index C_e values obtained form the Hostun sand assembles reported in the literature and those obtained from the synthetic particle assembles

Data source	Data type	Compression index (C_c)	Recompression index (C_e)
Present study for printed particles	Virgin compression	0.123	
	Unloading at 10% strain		0.022
	Recompression at 7.8% strain	0.238	
	Unloading at 19% strain		0.072
Colliat-Dangus [8] (Ph.D. thesis)	Virgin compression	0.230	
	Unloading at 20 MPa		0.013
Lancelot et al. [22] (isotropic compression)	Virgin compression	0.115	
	Unloading at 1 MPa		0.020

7 Conclusion

This article highlights an reproducible and open-source prototype that incorporates 3D printers to generate reproducible multiscale data to support the calibration and validation of micro-mechanical discrete mechanics models for granular materials. Since the shape, form, size and mechanical properties of the synthetic particles can be altered or controlled in a limited sense, this new degree of control may provide unprecedented opportunities to calibrate geo-mechanical models or to test, falsify and check hypotheses with controlled experiments.

It should be noted that our goal of this work is not manufacturing synthetic sand assembles as close to the real sand counterpart as possible, as those work already reviewed in this paper. Rather, our goal is to leverage 3D printing technique to generate supporting evidences such that claims on any invented discrete element model can be falsified by controlled tests that are open source, transparent, and can be easily shared to third party. Furthermore, it should be clarified that a falsified model does not necessarily be totally abandoned. In fact, the identification of the limitations of the model might make it more useful for the right applications. On the other hand, a model, claim, or hypothesis that is not falsifiable cannot be tested rigorously, despite of the fact that supportive evidences can be found.

Appendix: Analysis of microscopic responses

To investigate the grain rearrangements and porosity reduction phenomena at the microscopic scale, discrete DIC (cf. Ando et al. [2], Hall et al. [15], Tudisco et al. [44]) with image interpolation, has been performed on reconstructed image stacks of printed particle specimen at different stages of applied strain. In the DDIC process, firstly, each particle in the image stack representing the initial state of the specimen is labeled and named as reference

image stack. The relative position all other particles in image stacks representing different strain levels are then calculated via a particle tracking algorithm called Tomo-Warp2 (cf. Tudisco et al. [45]) developed in laboratory 3SR. The output results (displacement and rotation in all of three axial directions) are recorded in a spreadsheet for all particles in the specimen at different mechanical loading stages.

Figure 8 presents vertical displacement (Z direction) map obtained for 6 different stress states of the specimen (as presented in Fig. 6b) through a color pattern of the image slice cut through the middle of reference image stack (see Fig. 6a). The intensity of the color represents the relative movement of a particle in a particular stress state to that of in reference image stack. These 6 stress states are representative of particle position in (a) low strain level (scan 5), (b) loading/unloading at small (scan 9 and 10) and higher strain levels (scan 15 and 16) and, (c) high strain level (scan 18). Notably, since the concept of DDIC presents the relative position w.r.t. the reference image; therefore, all image slices in Fig. 8 are of reference image where different color intensity is representative of vertical displacement at mentioned strain level (via scan number).

At the first glance, this color map shows the significant movement of particles present near moving the piston (bottom layer). The movement is further shifted to middle and then top layer particles in due course of mechanical loading. This behavior resembles that of the theory of stress distribution in granular material and thus justifies the potential of particle tracking technique as well as of the synthetic material for such mechanical investigations. However, DDIC results showed some error as the negative displacement of higher magnitude for grains present in top and bottom interfaces. This observation is again due to "search window" error for some grains present in the interface [2].

Following a similar guideline, the 3D rotation measurements for the printed particles were made using the same strategy of DDIC (cf. Andò et al. [1]); providing data for each grain's rotation in all three axes (as a rotation vector) w.r.t. the reference image stack. The norm of these three rotation vectors was then calculated to represent 3D rotation. Similar to Fig. 8, the color map for same 6 stress states for 3D rotation has been presented in Fig. 9. The color intensity of each particle represents 3D rotation calculated as "norm" of rotation vector in all three directions.

The color map does not exhibit any traceable trend for the 3D rotation. However, the particles in the bottom layer are rotating more at the low strain levels whereas bottom and middle layer particles rotate significantly at the higher strain states. Top layer particles are merely leading to any sort of rotation. Further, the particle movement trends
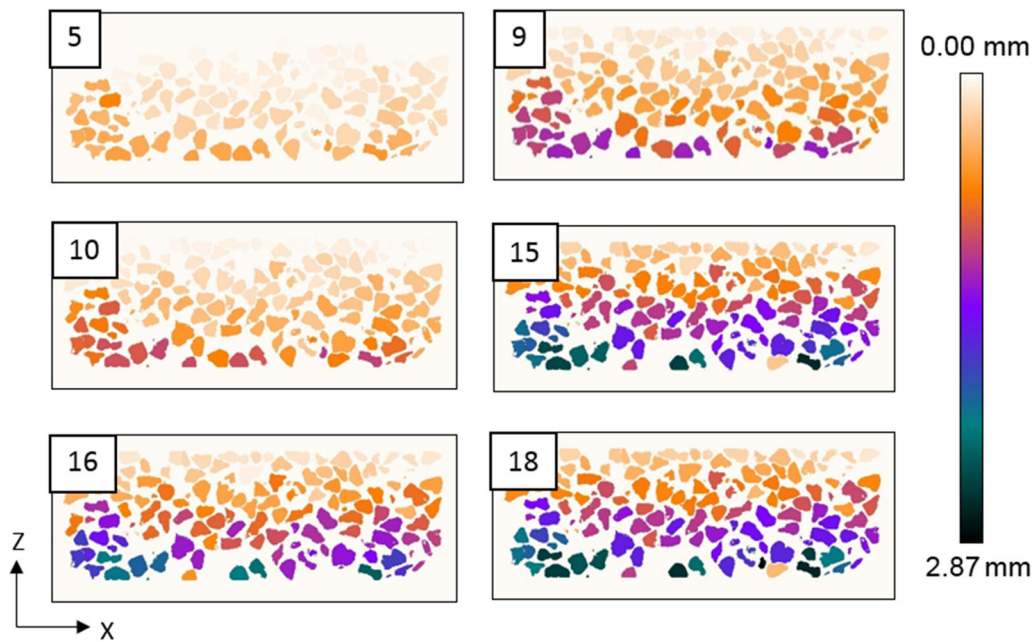
Fig. 8 Display of particle vertical displacement in form of color pattern in reference image slice

presented in Figs. 7 and 8 do not indicate the onset of deformation band or material bifurcation.

Therefore, in order to better understand the behavior quantitatively, few representative grains were selected from the bottom, middle and top layers of the vertical slice (see Fig. 6a for this) and their movement data over the course of loading is statistically demonstrated. Figure 10 presents this labeled vertical slice showing the chosen grains. Here, grains colored as "red" represent bottom layer, "green" represents middle and "blue" represents top layer. The labeled number represents the index of that particular grain in the sample.

Moreover, the quantitative movement information about these grains over the course of loading is presented graphically for the same 6 chosen stress states as presented in the previous section. Figure 11a below presents the data
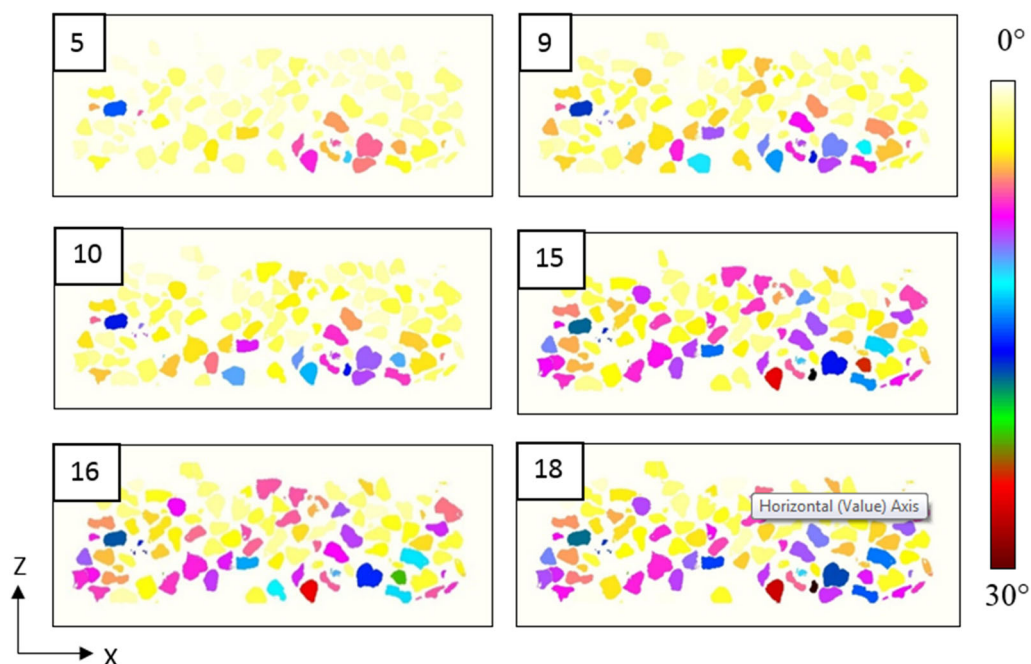

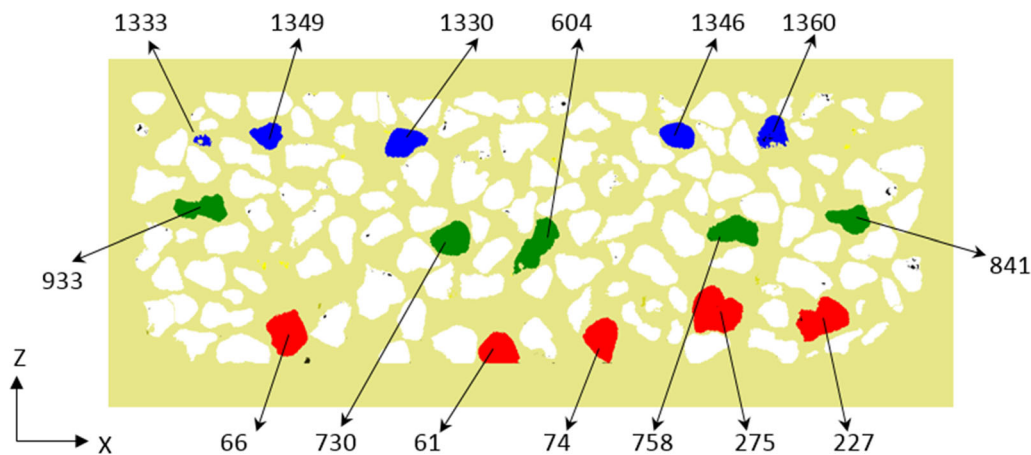**Fig. 9** 3D rotation (norm) map for printed particles at different loading stages

Fig. 10 Vertical slice from reference image stack presenting labeled grains from bottom (red), middle (green), and top (blue) layers for statistical particle tracking (color figure online)
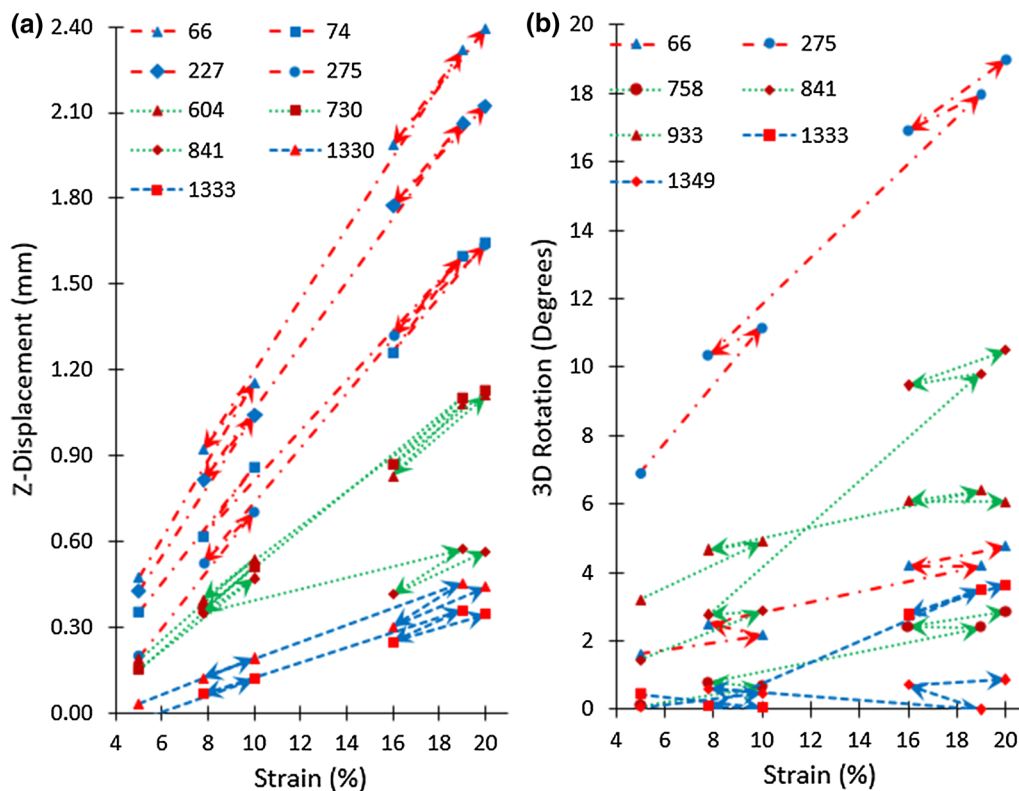

Fig. 11 Statistical representation of few selected grain indices for **a** vertical displacement, **b** 3D rotation

for vertical displacement for the few out of all marked grains in Fig. 10 where the color of trend line resembles with that of the layer it represents. Figure 11b presents the data for 3D grain rotation respecting the color code as used before.

Now, it is interesting to see the movement of grains in their respective layers. The vertical displacement is highest in magnitude followed by middle and lastly the top layer. This information was also visible on the color map shown

in Fig. 9. However, the plot (see Fig. 11a) provides additional information on the rate of displacement which follows the same trend of being highest for the bottom layer and lowest for the top. Also, the grains in bottom layer show higher heterogeneity in granular movement as presented by the wider range of vertical displacement. The middle and top layer grains, on the other hand, displace rather more homogeneously.

In the similar context, the data presented in Fig. 11b for 3D grain rotation show a random behavior for all grains rotating up to 10 degrees during the course of loading; except one-grain index "275" which exceptionally show larger grain rotation. Notably, as all grains show very random behavior for 3D rotation, only a few grains are presented in Fig. 11b for better readability. The almost constant granular rotation can be attributed to parameters like granular packing, coordination numbers, and neighbor count. Also, exceptionally higher values observed for one mentioned grain can be attributed to grain dislocations due to heterogeneity in void space. Subsequently, this kind of information holds the potential to aid standard DE techniques for contact detection, calculation of force-deformation and particle movement.

Similarly, the particle movement data for displacement in for X and Y directions has been evaluated from DDIC. Since the test performed was oedometric and therefore as such, no significant statistical information can be withdrawn from these measurements. Nevertheless, the data obtained for X and Y displacements is capable of has the capability to aid the calibration of DEM models and further their statistical representation will be significant for triaxial tests which can be studied in future.

In addition, Fig. 11 presents significant analytical information for vertical displacement whereas the trend for 3D rotation was quite random. Hence, we further analyzed the vertical displacement behavior choosing a large number of grains (instead of very few to be representative) for reliable and more promising observations. Four number of vertical levels (X–Y slices) were chosen from the specimen (as shown in Fig. 12, left) to evaluate the average vertical displacement of the grains present in these slices over the course of mechanical loading.

The X–Y plane slice in Fig. 12 (right) presents the section of the grains present in those slices in a general

context. The top and bottom slices (slice 4 and 1) are 1.94 mm offset from sample extremes and two middle slices (slice 2 and 3) are 3.88mm offset each from slice 4 and 1 toward the center of the sample. The top and bottom offset are chosen to avoid wrong measurements in interfaces because of search window [2] error (see Sect. 6 for details). The average vertical displacement was evaluated for the grains present in these 4 slices over the full course of mechanical loading (see Fig. 6b for details). The average vertical displacement map is presented below in Fig. 13. It can be clearly seen that the "slice 1" grains displace more and at the highest rate in comparison with others. This trend is neatly followed by the other three slices with lesser displacement and at a lower rate from
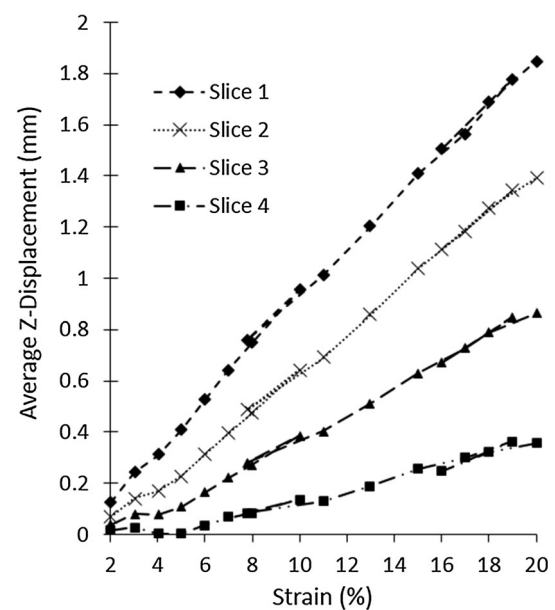

Fig. 13 Average vertical displacement plot over the course of mechanical loading for selected four X–Y slices
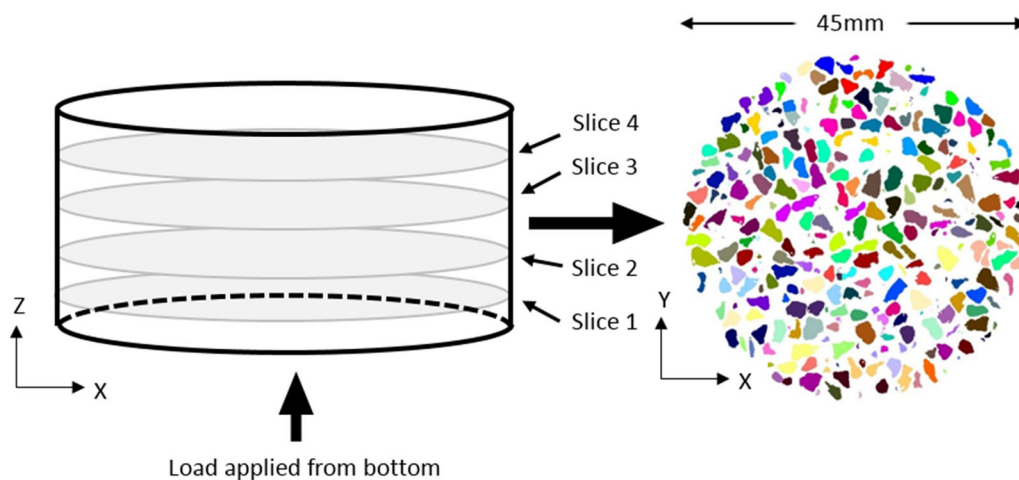

Fig. 12 Sketch of specimen presenting the four chosen X–Y slices (left), and a general section view of grain assembly in these slices (right)

"slice 2" to "slice 3" and finally "slice 4." This trend more rationally justifies the observations presented in Sect. 7 about the theory of stress distribution in granular materials. In addition, the trend is similar to the one presented in Fig. 11a with one major difference of data set, and thus more reliable conclusions can be drawn from Fig. 13. This further indicated the significance of particle tracking information for statistical analysis of mechanical behavior at the particle scale.

As a whole, the particle tracking data obtained in this study holds a tremendous amount of information to aid DEM modal calibration, fine-tuning of parameters and to positively describe the macroscopic behavior more rationally and confidently. This potential is also in line with our goal to provide an open-source database for researchers to verify and calibrate their DEM or FEM-DEM models.

References

1. Andò E, Hall S, Viggiani G, Desrues J, Bésuelle P (2012) Experimental micromechanics: grain-scale observation of sand deformation. Géotech Lett 2(3):107–112

2. Andò E, Hall SA, Viggiani G, Desrues J, Bésuelle P (2012) Grain-scale experimental investigation of localised deformation in sand: a discrete particle tracking approach. Acta Geotech 7(1):1–13

3. Andrade JE, Avila CF, Hall SA, Lenoir N, Viggiani G (2011) Multiscale modeling and characterization of granular matter: from grain kinematics to continuum mechanics. J Mech Phys Solids 59(2):237–250

4. Andrade JE, Lim K-W, Avila CF, Vlahinić I (2012) Granular element method for computational particle mechanics. Comput Methods Appl Mech Eng 241:262–274

5. Athanassiadis AG, Miskin MZ, Kaplan P, Rodenberg N, Lee SH, Merritt J, Brown E, Amend J, Lipson H, Jaeger HM (2014) Particle shape effects on the stress response of granular packings. Soft Matter 10(1):48–59

6. Azeiteiro RJ, Coelho PA, Taborda DM, Grazina JC (2017) Critical state-based interpretation of the monotonic behavior of Hostun sand. J Geotech Geoenviron Eng 143(5):04017004

7. Cho GC, Dodds J, Santamarina JC (2004) Particle shape effects on packing density. Stiffness and Strength of Natural and Crushed Sands-Internal Report, Georgia Institute of Technology

8. Colliat-Dangus J-L (1986) Comportement des matériaux granulaires sous fortes contraintes: influence de la nature minéralogique du matériau étudié. Ph.D. thesis, Grenoble 1

9. Cundall PA, Strack ODL (1979) A discrete numerical model for granular assemblies. Geotechnique 29(1):47–65

10. Desrues J, Viggiani G (2004) Strain localization in sand: an overview of the experimental results obtained in Grenoble using stereophotogrammetry. Int J Numer Anal Methods Geomech 28(4):279–321

11. Fang Q, Boas DA (2009) Tetrahedral mesh generation from volumetric binary and grayscale images. In: IEEE international symposium on biomedical imaging: from nano to macro, 2009. ISBI'09. IEEE, pp 1142–1145

12. Favier JF, Abbaspour-Fard MH, Kremmer M, Raji AO (1999) Shape representation of axi-symmetrical, non-spherical particles

13. Flavigny E, Desrues J, Palayer B (1990) Note technique: le sable d'hostun RF. Revue française de géotechnique 53:67–70

14. Friedman JH (1997) On bias, variance, 0/1—loss, and the curse-of-dimensionality. Data Min Knowl Discov 1(1):55–77

15. Hall SA, Bornert M, Desrues J, Pannier Y, Lenoir N, Viggiani G, Bésuelle P (2010) Discrete and continuum analysis of localised deformation in sand using X-ray μCT and volumetric digital image correlation. Géotechnique 60(5):315–322

16. Hanaor AH, Gan Y, Revay M, Airey DW, Einav I (2016) 3D printable geomaterials. Géotechnique 66:323–332

17. Henann DL, Kamrin K (2013) A predictive, size-dependent continuum model for dense granular flows. Proc Natl Acad Sci 110(17):6730–6735

18. Johnson KL (1987) Contact mechanics. Cambridge University Press, Cambridge

19. Katagiri J, Matsushima T, Yamada Y (2010) Simple shear simulation of 3D irregularly-shaped particles by image-based DEM. Granul Matter 12(5):491–497

20. Keller T, Lamandé M, Schjønning P, Dexter AR (2011) Analysis of soil compression curves from uniaxial confined compression tests. Geoderma 163(1):13–23

21. Kuhn MR, Sun W, Wang Q (2015) Stress-induced anisotropy in granular materials: fabric, stiffness, and permeability. Acta Geotech 10(4):399–419

22. Lancelot L, Shahrour I, Al Mahmoud M (2003) Experimental study of sand behaviour at low stresses. In: Di Benedetto et al (eds) Deformation characteristics of geomaterials. Swets & Zeitlinger B.V., Lisse, The Netherlands, pp 655–662

23. Liu Y, Sun W, Yuan Z, Fish J (2015) A nonlocal multiscale discrete-continuum model for predicting mechanical behavior of granular materials. Int J Numer Methods Eng 106:129–160

24. Liu Y, Sun W, Fish J (2016) Determining material parameters for critical state plasticity models based on multilevel extended digital database. J Appl Mech 83(1):011003

25. Matuttis HG, Nobuyasu Ito, Alexander Schinner (2003) Effect of particle shape on bulk-stress–strain relations of granular materials. In: Proceedings of RIMS symposium on mathematical aspects of complex fluids III, RIMS Kokyoroku series, vol 1305, pp 89–99

26. Miskin MZ, Jaeger HM (2013) Adapting granular materials through artificial evolution. Nat Mater 12(4):326–331

27. Ng T-T (2006) Input parameters of discrete element methods. J Eng Mech 132(7):723–729

28. Nouguier-Lehon C, Cambou B, Vincens E (2003) Influence of particle shape and angularity on the behaviour of granular materials: a numerical analysis. Int J Numer Anal Methods Geomech 27(14):1207–1226

29. Oda M, Konishi J, Nemat-Nasser S (1982) Experimental micromechanical evaluation of strength of granular materials: effects of particle rolling. Mech Mater 1(4):269–283

30. Oda M, Nemat-Nasser S, Konishi J (1985) Stress-induced anisotropy in granular masses. Soils Found 25(3):85–97

31. Ouhbi N, Voivret C, Perrin G, Roux JN (2017) 3D particle shape modelling and optimization through proper orthogonal decomposition. Granul Matter 19(4):86

32. Pena AA, Garcia-Rojo R, Herrmann HJ (2007) Influence of particle shape on sheared dense granular media. Granul Matter 9(3–4):279–291

33. Pestana JM, Whittle AJ, Salvati LA (2002) Evaluation of a constitutive model for clays and sands: Part I—sand behaviour. Int J Numer Anal Methods Geomech 26(11):1097–1121

34. Sadrekarimi A, Olson SM (2011) Critical state friction angle of sands. Géotechnique 61(9):771–783

35. Santamarina JC, Cho GC (2001) Determination of critical state parameters in sandy soils—simple procedure. Geotech Test J 24:185–192

36. Schneider CA, Rasband WS, Eliceiri KW (2012) NIH image to ImageJ: 25 years of image analysis. Nat Methods 9(7):671

37. Schofield A, Wroth P (1968) Critical state soil mechanics, vol 310. McGraw-Hill, London

38. Shin H, Santamarina JC (2012) Role of particle angularity on the mechanical behavior of granular mixtures. J Geotech Geoenviron Eng 139(2):353–355

39. Sun W, Andrade JE, Rudnicki JW (2011) Multiscale method for characterization of porous microstructures and their impact on macroscopic effective permeability. Int J Numer Methods Eng 88(12):1260–1279

40. Sun W (2013) A unified method to predict diffuse and localized instabilities in sands. Geomech Geoeng 8(2):65–75

41. Sun W, Wong TF (2018) Prediction of permeability and formation factor of sandstone with hybrid lattice Boltzmann/finite element simulation on microtomographic images. Int J Rock Mech Min Sci 106:269–277

42. Sun W, Andrade JE, Rudnicki JW, Eichhubl P (2011) Connecting microstructural attributes and permeability from 3D tomographic images of in situ shear-enhanced compaction bands using multiscale computations. Geophys Res Lett 38(10):L10302

43. Sun W, Kuhn MR, Rudnicki JW (2013) A multiscale DEM-LBM analysis on permeability evolutions inside a dilatant shear band. Acta Geotech 8(5):465–480

44. Tudisco E, Hall SA, Charalampidou EM, Kardjilov N, Hilger A, Sone H (2015) Full-field measurements of strain localisation in sandstone by neutron tomography and 3D-volumetric digital image correlation. Phys Procedia 69:509–515

45. Tudisco E, Andò E, Cailletaud R, Hall SA (2017) Tomowarp2: a local digital volume correlation code. SoftwareX 6:267–270

46. Wadell H (1935) Volume, shape, and roundness of quartz particles. J Geol 43(3):250–280

47. Wang B, Chen Y, Wong T (2008) A discrete element model for the development of compaction localization in granular rock. J Geophys Res Solid Earth 113(B3):B03202

48. Wang K, Sun W (2015) Anisotropy of a tensorial Bishop's coefficient for wetted granular materials. J Eng Mech 143:B4015004

49. Wang K, Sun W (2016) A semi-implicit discrete-continuum coupling method for porous media based on the effective stress principle at finite strain. Comput Methods Appl Mech Eng 304:546–583

50. Wang K, Sun W (2016) A semi-implicit micropolar discrete-to-continuum method for granular materials. In: Papadrakakis M, Papadopoulos V, Stefanou G, Plevris V (eds) Proceedings of European Congress on computational methods in applied science and engineering, June, pp 5–10, Crete Island

51. Wang K, Sun W (2018) A multiscale multi-permeability poroplasticity model linked by recursive homogenizations and deep learning. Comput Methods Appl Mech Eng 334:337–380

52. Wang K, Sun W, Salager S, Na S, Khaddour G (2016) Identifying material parameters for a micro-polar plasticity model via X-ray micro-computed tomographic (CT) images: lessons learned from the curve-fitting exercises. Int J Multiscale Comput Eng 14(4):389–413

53. Wood DM (1990) Soil behaviour and critical state soil mechanics. Cambridge University Press, Cambridge

54. Xu YF, Sun DA (2005) Correlation of surface fractal dimension with frictional angle at critical state of sands. Geotechnique 55(9):691–695